Journal of Asian Earth Sciences 75 (2013) 26–35

Contents lists available at SciVerse ScienceDirect

Journal of Asian Earth Sciences

journal homepage: www.elsevier.com/locate/jseaes

S-wave velocity images of the Dead Sea Basin provided by ambient seismic noise

José Badal [a,*], Yun Chen [b], Mimoun Chourak [c], Jacek Stankiewicz [d]

[a] Physics of the Earth, Sciences B, University of Zaragoza, Pedro Cerbuna 12, 50009 Zaragoza, Spain
[b] State Key Laboratory of Lithospheric Evolution, Institute of Geology and Geophysics, Chinese Academy of Sciences, Beijing 100029, PR China
[c] Département de Géologie, Faculté Pluridisciplinaire de Nador, Université Mohammed Premier, B.P. 300 Selouane, 62700 Nador, Morocco
[d] Deutsches GeoForschungsZentrum – GFZ, Telegrafenberg, 14473 Potsdam, Germany

ARTICLE INFO

Article history:
Received 14 March 2013
Received in revised form 7 June 2013
Accepted 27 June 2013
Available online 12 July 2013

Keywords:
Ambient seismic noise
Correlation
Dispersion
Tomography
Depth-dependent shear velocity models
Dead Sea

ABSTRACT

Based on passive seismic interferometry applied to ambient seismic noise recordings between station pairs belonging to a small-scale array, we have obtained shear wave velocity images of the uppermost materials that make up the Dead Sea Basin. We extracted empirical Green's functions from cross-correlations of long-term recordings of continuous data, and measured inter-station Rayleigh wave group velocities from the daily correlation functions for positive and negative correlation time lags in the 0.1–0.5 Hz bandwidth. A tomographic inversion of the travel times estimated for each frequency is performed, allowing the laterally varying 3-D surface wave velocity structure below the array to be retrieved. Subsequently, the velocity-frequency curves are inverted to obtain S-wave velocity images of the study area as horizontal depth sections and longitude- and latitude-depth sections. The results, which are consistent with other previous ones, provide clear images of the local seismic velocity structure of the basin. Low shear velocities are dominant at shallow depths above 3.5 km, but even so a spit of land with a depth that does not exceed 4 km is identified as a salt diapir separating the low velocities associated with sedimentary infill on both sides of the Lisan Peninsula. The lack of low speeds at the sampling depth of 11.5 km implies that there are no sediments and therefore that the basement is near 10–11 km depth, but gradually decreasing from south to north. The results also highlight the bowl-shaped basin with poorly consolidated sedimentary materials accumulated in the central part of the basin. The structure of the western margin of the basin evidences a certain asymmetry both whether it is compared to the eastern margin and it is observed in north–south direction. Infill materials down to ~8 km depth are observed in the hollow of the basin, unlike what happens in the north and south where they are spread beyond the western Dead Sea shore.

1. Introduction

The shear wave velocity is usually measured *in situ* by means of various invasive (borehole) or non-invasive techniques. Although these techniques provide accurate and well-resolved values of S-wave velocity (Badal et al., 2004) they suffer from several drawbacks, such as increasing costs with required depth or only pointwise estimates. In the last decades, passive seismic methods based on surface waves have received considerable attention by the seismologists. The success of these applications is explained by the fact that the ambient seismic noise wavefield consists primarily of surface waves (Campillo and Paul, 2003; Shapiro and Campillo, 2004; Wapenaar, 2004). The expression 'ambient seismic noise' is a generic term for both low- and high-frequency components. Cultural activities are the source of high-frequency signals, also called microtremors, whereas oceanic and atmospheric disturbances result in low-frequency signals or microseisms.

Since the beginning of this century the seismic interferometry techniques have rapidly become popular in a variety of applications (see reviews by Campillo, 2006; Curtis et al., 2006; Wapenaar et al., 2008; Schuster, 2009; Snieder et al., 2009). In particular, surface wave tomography using ambient noise is a rapidly expanding technique. The reason for its growing popularity is that it provides significant advantages compared to conventional earthquake tomography. It can be applied to regions with sparse or unevenly distributed or even non-existent seismicity. It produces reliable measurements at very low periods that are particularly difficult using earthquakes or explosions due to scattering and attenuation, which result in surface wave dispersion maps with high horizontal resolution that can be correlated with features of the upper crust. Another advantage of the ambient noise tomography over

* Corresponding author. Tel.: +34 976 761139.
E-mail addresses: badal@unizar.es (J. Badal), yunchen@mail.iggcas.ac.cn (Y. Chen), mchourak00@gmail.com (M. Chourak), jacek@gfz-potsdam.de (J. Stankiewicz).

1367-9120/$ - see front matter © 2013 Elsevier Ltd. All rights reserved.
http://dx.doi.org/10.1016/j.jseaes.2013.06.017

traditional earthquake tomography is the ability to estimate uncertainties based on the repeatability of the measurements.

One of the most intriguing aspects demonstrated both theoretically and experimentally, is that a random, isotropic ambient noise wavefield has correlations, which, on average, take the form of the Green's function of the medium, except for an additive phase factor which does not affect the group velocity measurements (Rickett and Claerbout, 1999; Lobkis and Weaver, 2001; Snieder, 2004; Wapenaar, 2004; Sabra et al., 2005a; Sánchez-Sesma and Campillo, 2006). Between pairs of receivers, the Green's function can be extracted from cross-correlations of long-time continuous records of ambient seismic noise registered at both receivers, in turn allowing an estimate of the propagation delay between the stations. The idea of extracting coherent signal by cross-correlation of noise was initially applied to seismic waves in helioseismology (Duwall et al., 1993). Weaver and Lobkis (2004) extracted Green's function by cross-correlating diffuse fields, and the response was favorably compared to direct Rayleigh waves. This development led to Shapiro and Campillo (2004) to cross-correlate vertical component records from seismic station pairs in North America to obtain Rayleigh waveforms. Since then the technique has generated a lot of interest across the globe; here we only cite some of the most relevant papers related to different regions in the world: southern California (Sabra et al., 2005b), Iceland (Gudmundsson et al., 2007), Baltic shield (Pedersen et al., 2007), northern Italy (Marzorati and Bindi, 2008), southern Africa (Yang et al., 2008), western United States (Lin et al., 2008), China (Zheng et al., 2008), Tibet (Yao and van der Hilst, 2009), Alps (Stehly et al., 2009), Australia (Saygin and Kennett, 2010), Mexico (Gaite et al., 2012), western Iberia (Silveira et al., 2013).

However, although many authors are largely using seismic noise to compute the empirical Green's functions between stations, we cannot lose sight that some theoretical and fundamental aspects are not well known nowadays. Theoretically, it has been demonstrated that the cross-correlation of diffuse wavefields is proportional to the imaginary part of the Green's function. This type of wavefield has some particular characteristics. For example, diffusion-like regimes can be obtained when the wavefield is generated by illumination with equipartitioned energy (Sánchez-Sesma et al., 2008, 2011). Whereas seismic coda waves present a diffuse behavior and their intensities decrease with time (Campillo and Paul, 2003), up to now the consideration of the seismic noise as a diffuse field is only a working hypothesis.

3D S-wave velocity images providing the local subsoil structure are of interest for geophysical prospecting in general and for earthquake engineering in particular, also for monitoring purposes. In this paper we present the seismic tomography of the Dead Sea obtained by seismic interferometry (cross-correlation) based on ambient noise and applied to recordings between station pairs belonging to a small-scale array deployed to this end. It is about a new study aimed to the migration of information from the frequency domain to the depth domain. We extracted empirical Green's functions from cross-correlations of long-term recordings. These functions contain Rayleigh waves whose group velocities are calculated in the microseismic bandwidth 0.1–0.5 Hz. We measured travel times of Rayleigh waves propagating between station pairs for different frequencies to later be inverted with the purpose of providing independent group-velocity sections. We followed an inversion procedure of Rayleigh wave velocity dispersion curves in order to obtain accurate images of the Dead Sea in terms of S-wave velocity at different depths.

2. The scenario and the data

The Dead Sea Transform, separating the African and Arabian plates, is one of the world's major transform faults. It extends for more than 1000 km in an approximate N-NNE orientation from the Red Sea Rift in the south to the Taurus-Zagros collision zone in the north. Since its inception about 18 Ma ago, it has experienced 105 km of lateral displacement (Quennell, 1958), being the recent relative plate motion of 3–5 mm per year (Klinger et al., 2000). Along its southern section, several basins of different sizes are found (Garfunkel, 1981; Garfunkel et al., 1981; Reches, 1987). The largest of them, about 150 km long and 15–20 km wide, is the Dead Sea Basin (DSB). Located between the Araba/Arava fault to the south and the Jericho fault to the north (Fig. 1a), it is one of the largest such features on Earth (Kashai and Croker, 1987). The longitudinal faults bordering the DSB are continuations of the major strike-slip faults north and south of the basin (Garfunkel and Ben-Avraham, 1996).

Following the success of the international multidisciplinary geoscientific project DESERT (Weber et al., 2004, 2009), the DEad Sea Integrated REsearch project (DESIRE) was launched in 2006, focusing on the DSB. Among the experiments carried out in the framework of the DESIRE project, 59 seismic stations were deployed in the Dead Sea region from October 2006 to March 2008. Most of the stations had short period sensors (1 Hz Mark L4 seismometers), though some broadband seismometers (Guralp 40-T, 3-T and Streckeisen STS2) were also used. The data recorded by broadband and short-period stations were digitized at 100 and 200 Hz, respectively. This network was designed with the main objective of studying the crustal structure around the DSB by recording local seismicity (Braeuer et al., 2009) and teleseismic events and receiver function analysis (Mohsen et al., 2011). On the topic at hand, continuous recordings over a period of months are necessary for a correct analysis of ambient noise. Unfortunately, not all locations had a recording station for the entire duration of the experiment, and there were a number of temporary and permanent instrument failures and cases of vandalism. Furthermore, the distribution of array stations should have been as uniform as possible to avoid any bias or ill-posed condition, but this rarely is so. After examining the quality of the recorded data we chose 20 stations for the analysis (Fig. 1a). Many ray-paths sampled the study area (Fig. 1b), thus minimizing the impact of diffraction-related errors and undesirable contributions coming from outside velocity anomalies. Five months of data were used, from May to September 2007.

Stankiewicz et al. (2012) have studied the ambient noise sources affecting the Dead Sea through frequency-time analysis and indentified the direction in which more energy is transmitted. It was observed that for a number of station pairs the direction from which the prominent signal arrived changed at a certain frequency. Previously, Stankiewicz et al. (2010) had already seen a similar reversal in Lake Toba, Sumatra. In our case this implies that the noise sources have different dominant frequencies in different directions. For station pairs separated in the north–south direction, the direction of the incoming signal switches around 0.2 Hz, such that lower frequencies come from the south, while higher frequencies originate in the north. This allows argue that the noise origin is most likely to be the Red Sea and the Mediterranean Sea, respectively (see review on this topic in Yang and Ritzwoller, 2008).

In this study the cross-correlation integral is calculated for the daily time series recorded at the 20 chosen stations, regardless of other techniques for signal extraction (e.g. see Schimmel et al., 2011). The success of the cross-correlation is due to waves which are recorded at a station pair and which add constructively at lag times that equal their propagation times between the station pair. The daily cross-correlation of the noise vertical component supplies the basic information from which we extract the Green's functions that lead to the Rayleigh waveforms traveling between the two stations concerned. In absence of data recorded continuously at a given station a day in particular (due to site maintenance

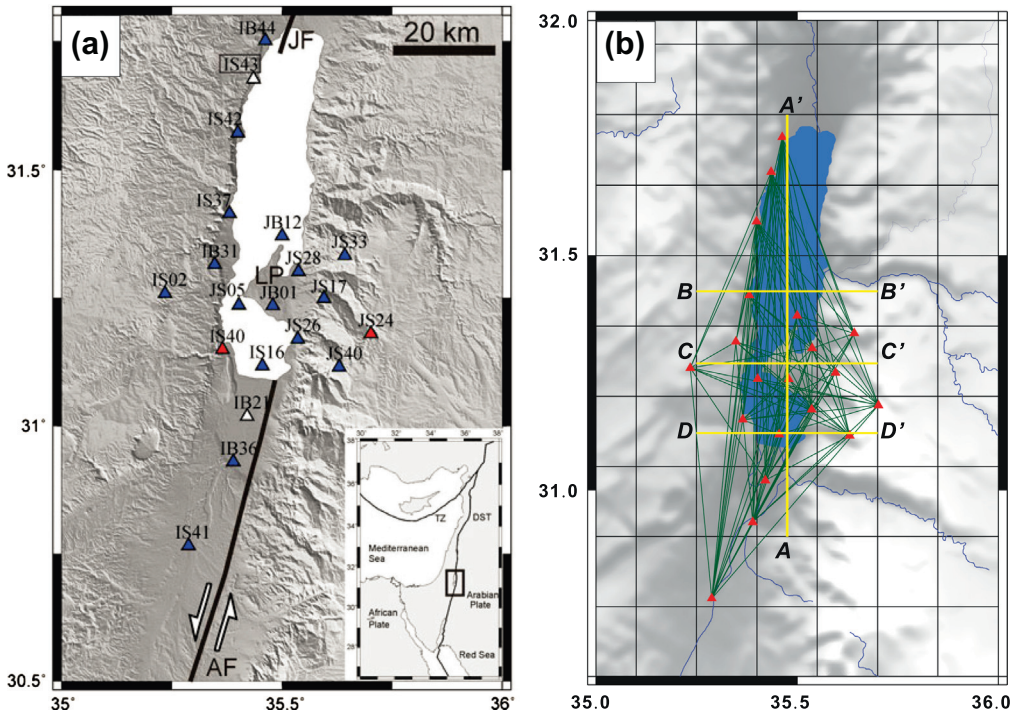

Fig. 1. (a) Setting map of the Dead Sea area showing the location of the 20 seismic stations (triangles) used in this study. Symbols: AF, Araba/Arava Fault; JF, Jericho Fault; LP, Lisan Peninsula. The inset shows the tectonic setting of the region. Station labeled as IS43 (to the north) is used as reference in Fig. 3. (b) Path coverage (straight lines) for Rayleigh waves propagating between stations and transects taken as references for vertical cross-sections of the study area that are shown later in Fig. 8. Transect A–A′ crosses the study region from north to south, while transects B–B′, C–C′ and D–D′ cross the Dead Sea from west to east.

or instrument failure), the recorded data were discarded. An optimized pre-processing of the signal not always is guarantee of more reliable results; nevertheless, we carry out a series of operations with this goal. Since we make use of broadband and short-period stations simultaneously, we applied a Butterworth high pass filter to all broadband recordings. This made the spectral responses of all stations similar; without this step the cross-correlations of signals from two different types of stations would be meaningless. Short period data recorded at 200 Hz were re-sampled to 100 Hz with the help of an antialising filter to be compatible with broadband data. Furthermore, any instrumental error that adds a linear bias to the record must be removed. Removing the mean of each daily record prior to cross-correlation is necessary for accurately estimating the amplitude of the signal. We divided the entire trace by the highest (absolute) value of the waveform, thus setting the amplitude to 1. If this normalization in time domain is not done, when microseismic noise is detected, a daily trace from a day with an earthquake will have much higher amplitude, and the cross-correlation function of these traces will also be much higher, and the stacking process will be contaminated by local and teleseismic events if not by non-stationary noise sources near the stations. Given that the ambient noise amplitude spectrum is not flat in the frequency band of interest, we carried out spectral 'whitening' consisting of dividing the full noise spectrum by the smoothed amplitude spectrum. This operation results in that all frequencies have comparable amplitudes, which reduces the effect of persistent monochromatic sources (Villaseñor et al., 2007). In Fig. 2 we show a flow chart that helps to understand at a glance the set of operations involved in the ambient seismic noise analysis.

For each available station pair, the resulting correlation function is a two-sided time function with both positive and negative correlation lags, which effectively describes the two directions in which signal travels between stations. Fig. 3 shows the cross-correlation of the signal recorded by station IS43 with all other stations, with seismic energy arriving at the time expected for surface waves. We stacked the daily correlation functions for each station pair to improve the signal to noise ratio.

3. Group velocity variation at different frequencies

After stacking the daily correlations to the desired number of days, the frequency dependent group velocities of the arrivals were calculated using frequency-time analysis (Ritzwoller and Levshin, 1998). We filtered each Green's function with progressively higher frequency range and computed the envelope of each resulting filtered trace. We then plotted these envelopes all together, as well as the arrival times across the frequency spectrum using predefined conditions regarding the theoretically possible velocities and the prominence of the arrival. Measurable Green's functions were observed in the frequencies between 0.1 and 0.5 Hz. Coherent arrivals could only be detected in this frequency range. We really did try to get as much information as possible, but are limited by the frequencies in which the noise is actually generated, as well as the instrumental response.

Travel times of Rayleigh waves between station pairs were measured at different frequencies within the range of interest, to then be inverted tomographically and so obtain group velocity variation for each frequency. To this end, we gridded the sampling region and we determined the slowness on each grid cell by tomographic inversion (Chen et al., 2010). We performed 2D inversions using different grid sizes. The models did not change significantly when other meshes of similar grid sizes were used. The results presented here were calculated on a $0.15^\circ \times 0.15^\circ$-sized grid. Fig. 4 shows the surface wave group velocity patterns obtained for different frequencies: 0.1, 0.2, 0.32 and 0.5 Hz. Rayleigh waves of different frequencies have different group velocities due to the fact they sample different depths, with lower frequencies

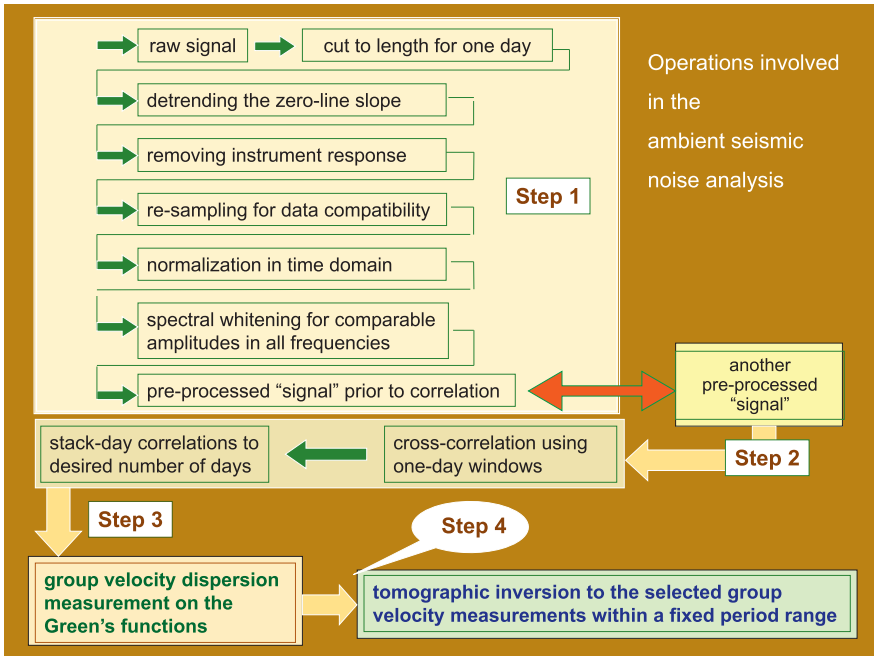

Fig. 2. Set of operations involved in the ambient seismic noise analysis (flow chart).

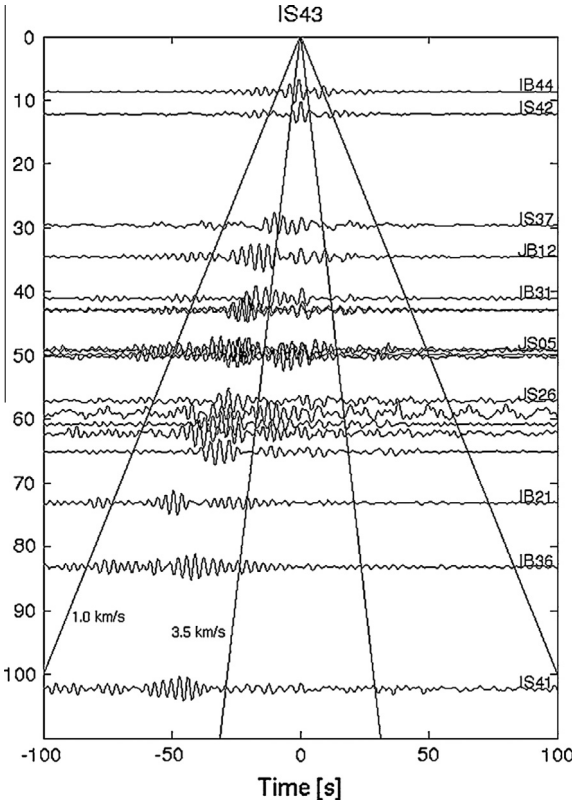

Fig. 3. Emergence of Rayleigh waveforms in the stacks of daily cross-correlations of the signal recorded by station IS43 with all other stations, plotted against the distance between stations. Straight lines show where arrivals corresponding to velocities between 1.0 and 3.5 km/s would be expected.

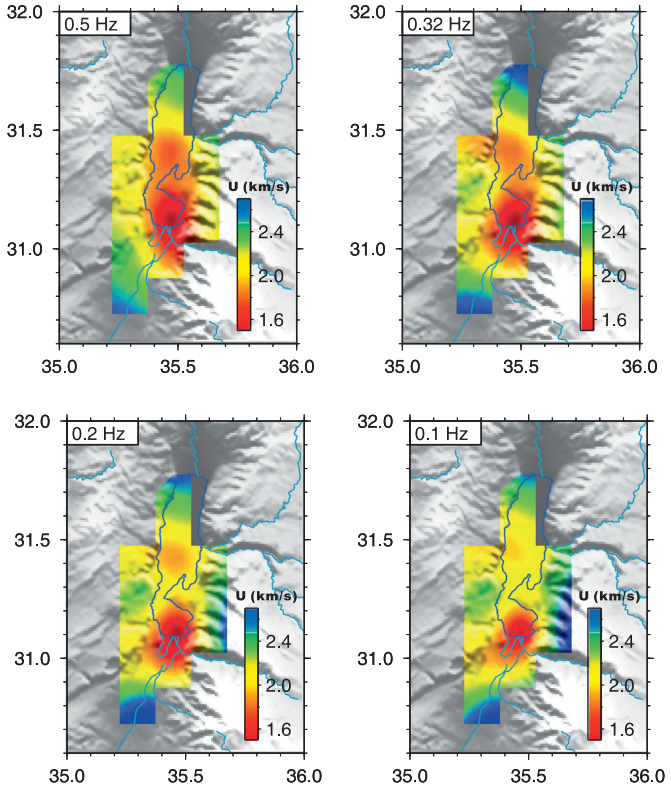

Fig. 4. Surface wave group velocity patterns obtained for different frequencies: 0.1, 0.2, 0.32 and 0.5 Hz.

penetrating deeper into the crust. The 0.5 Hz frequency samples the uppermost ~2 km, while the 0.1 Hz signal penetrates down to ~12 km.

4. Inversion of group velocities

Although the relationship between Rayleigh wave frequency and sampling depth is quite informative, the fact is that it is not straightforward. Hence our interest in inverting the velocity-frequency curves to obtain shear velocity-depth models and further

tomographic images of the study area, which will be displayed as horizontal depth sections and vertical sections.

4.1. Inversion approach (implementation)

We start with an initial velocity model without low-velocity layers that consists of a homogeneous half-space with constant shear velocity of 3.2 km/s. The velocities in this reference model are set to be larger than those plausible and the number of layers and depths to boundaries between them are inputs for computation. Therefore the initial model neither resembles nor reflects the actual structure.

We used a damped least-squares approach (Aki and Richards, 1980; Dimri, 1992) to invert group velocity dispersion. In this context, the best damping factor for implementation is determined from the trade-off between resolution and covariance. That is, the optimum damping factor is the one that offers higher resolution and lower covariance simultaneously. In Fig. 5 we have plotted the trade-off between resolution and covariance for different damping. We chose $s^2 = 0.0005$ as the optimum value for damping, in which case the covariance does not exceed 0.0004 km^2/s^4 and the resolution is very close to 0.5. As the biggest error affecting the surface wave travel times never exceeds 0.5 s (because of the very short distances travelled by the waves), then the error made in the determination of depth-dependent shear velocity is in any case less than 0.01 km/s (sqrt $(0.25 * 0.0004)$).

The initially assumed model is updated at each step of inversion so that the variance between observed and calculated group velocity is computed to check the convergence of the process. The procedure is repeated until the difference between the new shear velocity values at a specified grid node and the shear velocity values computed in the previous step converges to a minimum rms deviation in shear velocity of less than 0.001 km/s and a residual dispersion fitting of less than 0.02 km/s. The convergence of the process requires no more than fifteen successive iterations.

4.2. Variance reduction (reliability)

Fig. 6 shows an example of period-dependent surface wave velocity at the grid point of latitude 31.275°N and longitude 35.475°E, together with the best-fitting shear-wave velocity model obtained by inversion. The model that gives the least variance between observed and calculated group velocity is considered as final model at the target grid node. In Fig. 6a we compare the observed Rayleigh group velocity dispersion with the theoretical dispersion computed by forward modelling from the final velocity model, and we can see an excellent coincidence between both curves. In Fig. 6b the final shear velocity model appears completely differentiated from the initial model, as expected. The error bounds in shear velocity are indeed very small (in the third decimal place) and are not plotted in the velocity-depth models, as they are not visually relevant for further comparisons.

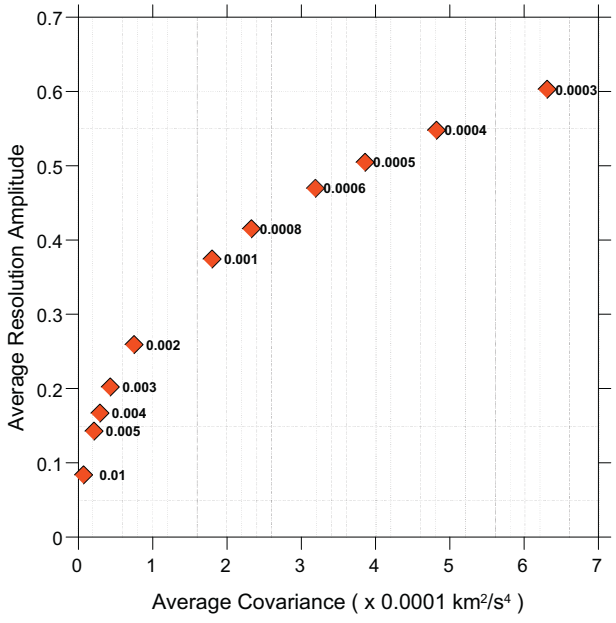

Fig. 5. Trade-off between covariance and resolution when using different damping factors for inverting Rayleigh wave group velocity dispersion.

4.3. Resolving kernels (quality)

The kernels (rows) of the resolution matrix of the inverse problem were calculated at various depths and reference grid points to illustrate the quality of the solution, since they are a measure of the accuracy achieved when the solution is calculated at a target grid node. In Fig. 6c we show the resolving kernels for the S-wave velocity model plotted in Fig. 6b. The kernels computed for other target nodes and short wavelengths are of similar quality. The sharper the peak of the kernel with respect to the baseline at each depth, the better the agreement between the final and actual models, and hence the greater the reliability of the inversion result. In our case, the Rayleigh waveforms transmitted by ambient seismic noise allow us to resolve down to ~11 km depth.

5. Tomographic images and basin structure

The 3D seismic velocity structure of the Dead Sea is displayed by: (a) S-wave velocity maps at various depths above the reliable depth interval for short-period Rayleigh waves (Fig. 7); (b) S-wave velocity cross-sections along a north–south profile A–A′ and three west-to-east profiles B–B′, C–C′ and D–D′ (Fig. 8). These latitude- and longitude-depth sections cross the northern, middle (Lisan Peninsula) and southern parts of the Dead Sea, respectively (Fig. 1b). Owing to the ray coverage near the basin edge, non-uniqueness of the solution, smoothing introduced at different stages of the inversion process and possible (although small) smearing effects, all of them constraints which plague the inversion process of waveforms, we make reference only to velocity variations on a limited scale and the main features of basin structure.

5.1. Horizontal slices

Fig. 7 shows tomographic images of the DSB as horizontal slices at six sampling depths, and thus together giving an overview of the velocity variation in 3D extending to a depth of 11.5 km. This is the deepest than can be resolved with the available frequency range that characterizes the Rayleigh waveforms used. Reliable maps for shallower depths would require a greater number of seismic stations, better azimuthal path coverage, shorter ray paths, i.e. smaller interstation distances or spacing and higher sampling rate; maps for deeper depths would require a greater penetration of the waves and therefore longer periods, and longer ray paths in order to enhance the signal-to-noise ratio.

The models here presented reveal shear velocities ranging between 1.8 and 3.0 km/s and gradually increasing as the depth increases. The lowest speeds are found at a sampling depth of 1.5 km and dominate the whole DSB; more precisely, the northern third of the Dead Sea area shows speeds between 2.3 and 2.8 km/s (although this part that lies northernmost was not well probed by the waves), while the southernmost two-thirds show

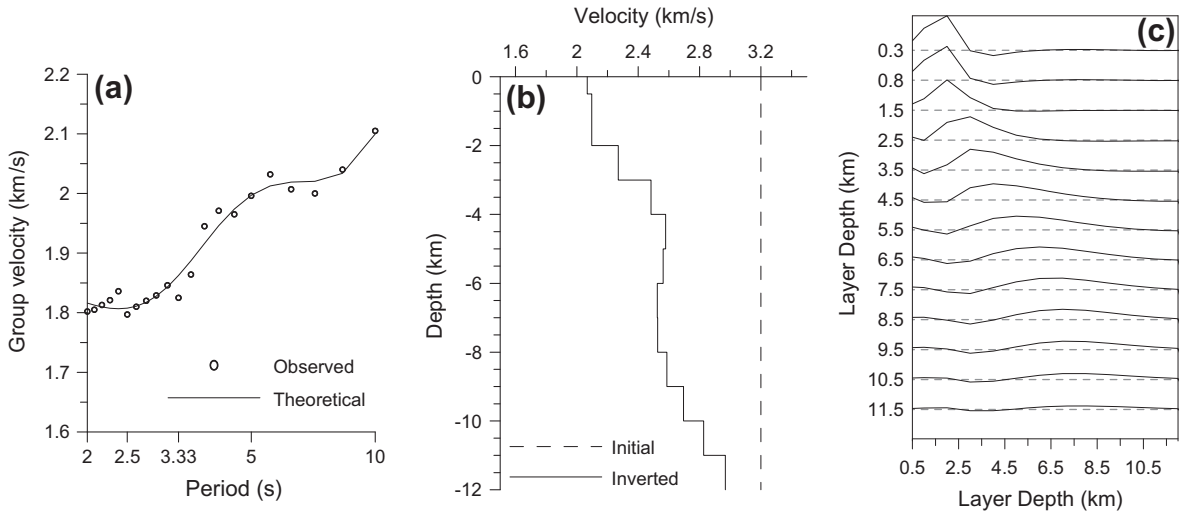

Fig. 6. Example of the results obtained when inverting period-dependent surface wave velocity at the grid point of latitude 31.275°N and longitude 35.475°E. (a) Observed (dots) and theoretical (continuous line) group velocity dispersion curves; the latter curve is computed by forward modeling from the final velocity-depth model achieved after the last iteration. (b) Best-fitting shear-wave velocity model (solid line) obtained by inversion together with the velocity profile (dash line) used as initial model for inversion. (c) Resolving kernels for the best-fitting velocity model.

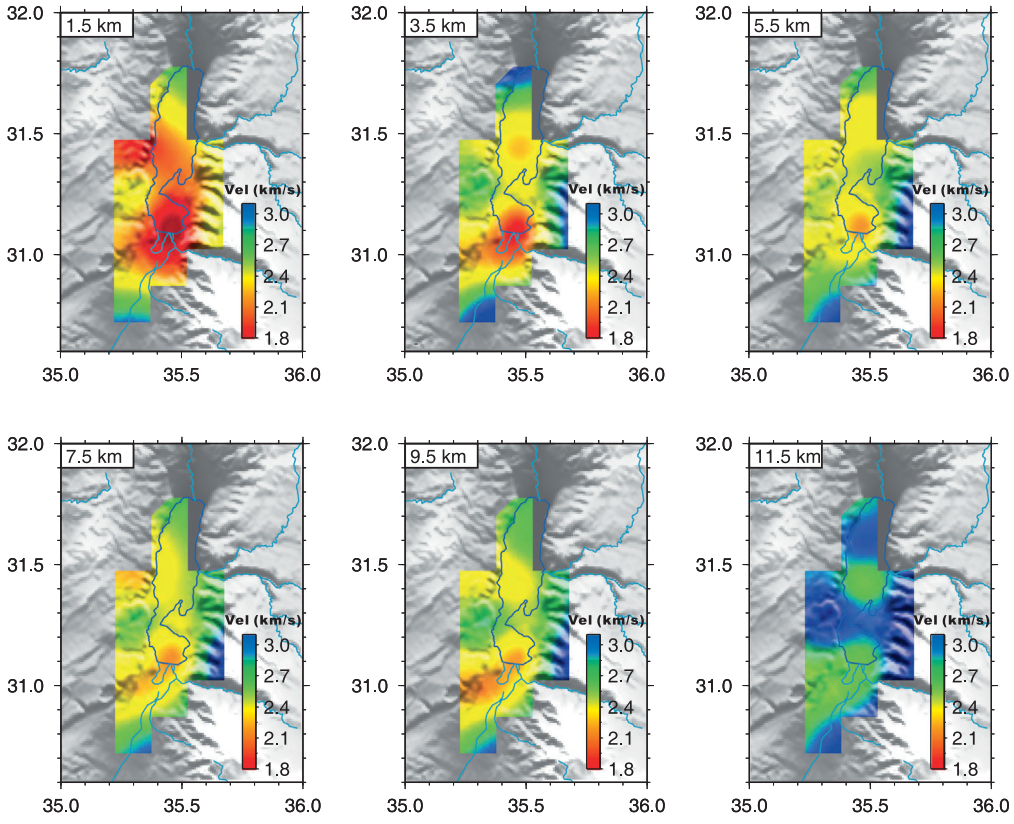

Fig. 7. Horizontal depth sections of the Dead Sea area computed for depths 1.5, 3.5, 5.5, 7.5, 9.5 and 11.5 km.

speeds from 1.8 to 2.2 km/s. In particular, a zone emerging south of the Lisan Peninsula at ~31.1°N is featured by so low velocity as 1.8 km/s. A similar velocity pattern can be seen at 3.5 km depth, although not so low values as before. However, now it is more evident a spit of land with speed 2.4 km/s, that starting from the small peninsula at ~31.3°N takes southwest direction and separates two low velocity zones on both sides north and south. This formation is the response to a concentration of low fluid content mass identified as the Lisan salt diapir (Stankiewicz et al., 2012), which separates the low velocities associated with sedimentary infill on both sides of the peninsula (at ~31.1°N and 31.45°N). The depth of this formation does not exceed 4 km, what seems agree with an early estimation by Garfunkel and Ben-Avraham (1996).

Moving away from the low-velocity zone, velocity increases rapidly to the east and west, and a bit more gradually northward and southward reaching values of 2.6 and 2.8 km/s on each side, respectively. At a depth of 5.5 km, even with similar shear-velocity

variation pattern, the velocities of the basin are already found above 2.3 km/s everywhere, with the exception of a remnant low-speed of 2.2 km/s in the same zone south of Lisan. This scheme, with similar lateral velocity changes, is kept at least to a depth of 9.5 km, from which speeds between 2.8 and 3.0 km/s already are a common feature for the whole area.

If we divide the DSB by an imaginary line from north to south through the middle of the basin, it is possible to appreciate a west–east asymmetry with comparatively higher speeds lying on the eastern margin of the basin, which highlights its asymmetrical shape. Also, a quite clear velocity contrast draws the attention when comparing the model at 9.5 km depth with the model at

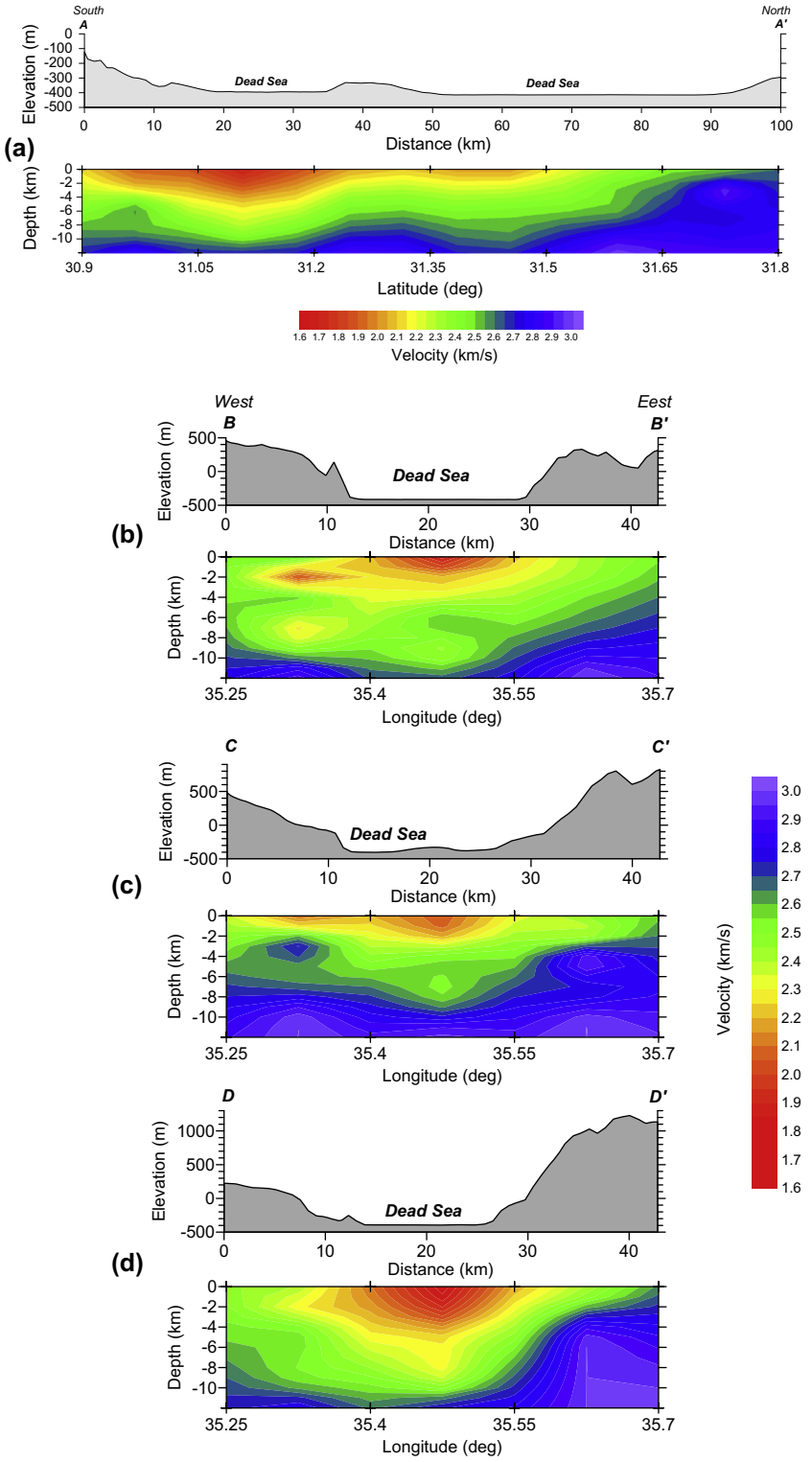

Fig. 8. Vertical sections of the Dead Sea area along the north-to-south transect A–A′ (a) and the west-to-east transects B–B′, C–C′, D–D′ (b–d) which cross the region by the north, middle (Lisan Peninsula) and south, respectively (Fig. 1b). In all cases the topographic relief has been included (top). The images are drawn by S-wave velocity isolines and according to the depth penetration of the models, and show velocity variations both laterally and with depth.

11.5 km depth. Being this change in velocity common to all the basin, the lack of a low velocity at this last reference depth means that there are no sediments and therefore that the basement in the DSB is at a depth near 10–11 km (at least in a large part of the basin), that still is a depth sampled by the surface waves.

5.2. Cross-sections at prefixed longitude and latitudes

Fig. 8a displays an overall view of the DSB along a north–south 100 km-long profile, from 30.9°N to 31.8°N, which includes the changes in shear velocity both laterally and with depth. The image reveals a suite of crustal layers with laterally varying speeds and gradually decreasing depths from south to north, above all in the northern third of the basin. A clear uplift is observed halfway of the profile coinciding with a slight elevation of the Dead Sea bottom, which can be attributed to the upthrust of the diapiric salt mass mentioned above. The basement in the DSB, represented by the isoline of ~2.8 km/s, can be now set at a depth of ~11 km along the 30 km further south; this depth becomes about 8–9 km at latitudes from 31.24°N to 31.32°N approximately, and then increases up to the same values that before, and from 31.47°N decreases continuously northward where speeds of up to 2.9–3.0 km/s appear at depths so shallow as 2–4 km. The remaining layers fit this same pattern with a horizontal velocity gradient so that the layer speeds are each time greater as we move northward. An evident dissimilarity is observed in the southern third of the basin with respect to the rest of it: sediments with speed so low as 1.8–1.9 km/s and above the depth of 3 km are found at latitudes that do not exceed ~31.23°N, just south of the Lisan salt diapir (this feature is also highlighted in the horizontal slices at 1.5 and 3.5 km depths).

Fig. 8b–d enable seeing three sections of the DSB at prefixed latitudes from north to south. The respective S-wave velocity patterns show clearly the bowl-shaped basin, the north–south variation in the inner velocity structure of the basin as well as the smoothly changing depth of the basement. Pure sedimentary infill (2.0–2.2 km/s) is present at depths not exceeding 3 km west of the northern part of the Dead Sea (Fig. 8b), and hardly 2 km west of the middle part of the basin (Fig. 8c), but also infill occupying a great part of the bowl (Fig. 8d). Very poorly consolidated sedimentary materials (2.1–2.2 km/s) are accumulated in the central part of the basin (especially with greater thickness to the south), which is also containing a bigger sediment deposit (speeds of 2.4–2.6 km/s) in comparison with the materials (2.7–2.8 km/s) in the basin edges and beyond (Fig. 8b–d).

The cross-section imaged in Fig. 8c goes through the Lisan Peninsula and illustrates the seismic velocity structure of the DSB at that latitude. Velocities of about 2.5–2.6 km/s are viewed down to a depth of ~8 km, filling completely the basin hollow, unlike what happens in the north and south where these speeds are spread beyond the western Dead Sea shore. The somewhat more complex structure of the western margin of the basin evidences a certain asymmetry both whether it is compared to the eastern margin and it is observed in north–south direction (Fig. 8b–d).

6. Brief discussion

We have regarded the low-velocity seismic signature in the DSB as the contrast element to set the basement of the basin, just where the vertical velocity gradient is more pronounced and speed increases significantly. The poorly consolidated materials having a low-velocity regime are interpreted as sedimentary infill associated with the formation of the basin. The results highlight an undulating basement at a depth close to 11 km, after 8–9 km, again about 11 km and finally at gradually decreasing depths as we move northward. This structural model is consistent with the P-wave velocity model derived from wide-angle seismic data by Mechie et al. (2009) for the southern DSB. These authors observed low velocities in the DSB down to depths of ~8 km; although the seismic basement was set at a depth of 11 km in relation to older and more compacted materials underlying the sedimentary infill. In turn, the basement depths are consistent with those determined from teleseismic P-wave tomography and gravity data by Hofstetter et al. (2000) and in earlier seismic studies (Al-Zoubi et al., 2002; Ten Brink et al., 2006).

Since salt comparatively exhibits higher seismic velocity (Ezersky, 2006), a spit of land at ~31.3°N is identified as a diapiric formation, the Lisan salt diapir, which separates the low velocities associated with the sedimentary infill on both sides north and south of the basin. The estimated depth of this formation is about 4 km (Figs. 7 and 8a) in agreement with Garfunkel and Ben-Avraham (1996). The less compacted material is always found in the central part of the DSB that encloses the poorly consolidated sediments along nearly 100 km long of the basin. Still more, the younger and most weathered sediments are around a narrow north–south band occupying just the central portion of the basin (Fig. 8b–d).

The extension of the low velocity zones westwards from the Dead Sea shore (Fig. 8b and d) is also reflected by the different faulting style on both borders of the basin caused by the transtensional deformation within the last 5 Myr. While the eastern margin of the DSB is formed by relatively simple dip-slip and strike-slip faults that separate the basin from the elevated Arabian Plate (Quennell, 1958), the structure of the western margin, a ~5 km wide belt, reflects normal faulting and is more complex (Zak and Freund, 1981; Sagy et al., 2003). These authors estimate the cumulative vertical displacement at 10 km or more. Gravity modeling (Ten Brink et al., 1993) confirms the asymmetrical shape of the basin, though it suggests that sediments are found off the western coast of the Dead Sea to depths not exceeding 5 km.

Recently, local earthquake data from a temporary seismic network installed in the southern Dead Sea area have been used to obtain the distribution of the P-wave velocity and the V_P/V_S ratio (Braeuer et al., 2012). The basin fill also shows an asymmetrical structure but now with an average depth of 7 km at the western boundary and between 10 and 14 km at the eastern boundary. This discrepancy, even keeping the shape and general features of the basin, may be due to the different sampled area (southern Dead Sea area versus the whole basin), the nature of the dataset used in each case (P- and S-arrival times versus Rayleigh wave travel times for positive and negative correlation time lags), and also to the working method applied (local earthquake tomography versus passive seismic interferometry). Even so, it is a point of controversy worthy of being studied more carefully.

7. Concluding remarks

The feasibility of the cross-correlation technique, when applied to ambient seismic noise recorded daily between station pairs belonging to an array in the Dead Sea region, has enabled us to extract surface waves in the secondary microseismic bandwidth 0.1–0.5 Hz and then achieve an accurate view of the seismic velocity structure of the Dead Sea Basin in all its extension. The results presented here depict a bowl-shaped basin containing sediment infill (lands of very low velocity) down to 4–5 km depth in the southern third of the basin and only 2 km in its middle third, with decreasing trend northward. Below this sediment shallow layer, materials a bit more consolidated (though still of low velocities) and with the same trend are found at depths of up to 11 km in the southern half and 8 km in the northern half.

The rapid transition to a higher velocity regime is interpreted as the basement, which is found at a depth close to 11 km in the south for then decreasing gradually northward. Being true that sedimentary infill is occupying the most part of the depression and is accumulated in its central part, however the basin shows a clearly asymmetrical structure with sedimentary materials above 10 km unevenly distributed on its western margin and beyond the Dead Sea shore in contrast to shallower sediments on its eastern margin.

Acknowledgements

The Geophysical Instrument Pool Potsdam (GIPP) provided the field instruments to carry out this experiment. The recorded data are stored in the Geofon Data Centre (http://geofon.gfz-potsdam.de/geofon). The scientific collaboration with the Deutsches GeoForschungsZentrum-GFZ of Potsdam, Germany, is highly valued. The National Natural Science Foundation of China partly funded this research (Grants 41074057, 41021063). The present work takes advantage of the Collaboration Agreement between the Institute of Geology and Geophysics, Chinese Academy of Sciences, Beijing, and the University of Zaragoza, Spain. The helpful comments and suggestions made by three anonymous reviewers helped to improve the manuscript greatly.

References

Aki, K., Richards, P.G., 1980. Quantitative Seismology: Theory and Methods. W.H. Freeman, San Francisco.

Al-Zoubi, A., Shulman, H., Ben-Avraham, Z., 2002. Seismic reflection profiles across the southern Dead Sea basin. Tectonophysics 346, 61–69.

Badal, J., Dutta, U., Serón, F., Biswas, N., 2004. Three-dimensional imaging of shear wave velocity in the uppermost 30 m of the soil column in Anchorage, Alaska. Geophysical Journal International 158, 983–997.

Braeuer, B., Weber, M., Asch, G., Haberland, C., Hofstetter, A., El-Kelani, R., Darwish, Y., 2009. Seismicity as a Key to Understanding the Dead Sea Transform Fault—Results from a Temporary Dense Seismic Network in the Southern Dead Sea basin. EOS Transactions, AGU, Fall Meeting Suppl. vol. 90, p. 52.

Braeuer, B., Asch, G., Hofstetter, R., Haberland, Ch., Jaser, D., El-Kelani, R., Weber, M., 2012. High-resolution local earthquake tomography of the southern Dead Sea area. Geophysical Journal International 191, 881–897, doi: 10.1111/j.1365-246X.2012.05668.x.

Campillo, M., Paul, A., 2003. Long-range correlations in the diffuse seismic coda. Science 299, 547–549.

Campillo, M., 2006. Phase and correlation in 'random' seismic fields and the reconstruction of the green function. Pure and Applied Geophysics 163, 475–502.

Chen, Y., Badal, J., Hu, J., 2010. Love and Rayleigh wave tomography of the Qinghai-Tibet Plateau and surrounding areas. Pure and Applied Geophysics 167 (10), 1171–1203. http://dx.doi.org/10.1007/s00024-009-0040-1.

Curtis, A., Gerstoft, P., Sato, H., Snieder, R., Wapenaar, K., 2006. Seismic interferometry – turning noise into signal. Leading Edge 25, 1082–1092.

Dimri, V., 1992. Deconvolution and Inverse Theory, Application to Geophysical Problems. Elsevier, Amsterdam.

Duwall, T.L., Jefferies, S.M., Harvey, J.W., Pomerantz, M.A., 1993. Time-distance Helioseismology. Nature 362, 430–432.

Ezersky, M., 2006. The seismic velocities of the Dead Sea salt applied to the sinkhole problem. Journal of Applied Geophysics 58, 45–58. http://dx.doi.org/10.1016/j.jappgeo.2005.01.003.

Gaite, B., Iglesias, A., Villaseñor, A., Herraiz, M., Pacheco, J.F., 2012. Crustal structure of Mexico and surrounding regions from seismic ambient noise tomography. Geophysical Journal International, doi: 10.1111/j.1365-246X.2011.05339.x.

Garfunkel, Z., 1981. Internal structure of the Dead Sea leaky transfrom (rift) in relation to plate kinematics. Tectonophysics 80, 81–108.

Garfunkel, Z., Zak, I., Freund, R., 1981. Active faulting in the Dead Sea rift. Tectonophysics 80, 1–26.

Garfunkel, Z., Ben-Avraham, Z., 1996. The structure of the Dead Sea basin. Tectonophysics 266, 155–176.

Gudmundsson, O., Khan, A., Voss, P., 2007. Rayleigh wave group velocity of the Icelandic crust from correlation of ambient seismic noise. Geophysical Research Letters 34, L14314. http://dx.doi.org/10.1029/2007GL030215.

Hofstetter, A., Dorbath, C., Rybakov, M., Goldshmidt, V., 2000. Crustal and upper mantle structure across the Dead Sea rift and Israel from teleseismic P-wave tomography and gravity data. Tectonophysics 327, 37–59.

Kashai, E.L., Croker, P.F., 1987. Structural geology and evolution of the Dead Sea–Jordan rift system as deduced from new subsurface data. Tectonophysics 141, 33–60.

Klinger, Y., Avouac, L., Dorbath, L., Karaki, N.A., Tisnerat, N., 2000. Seismic behaviour of the Dead Sea Fault along Araba valley, Jordan. Geophysical Journal International 142, 769–782.

Lin, F.-C., Moschetti, M.P., Ritzwoller, M.H., 2008. Surface wave tomography of the western United States from ambient seismic noise: Rayleigh and Love wave phase velocity maps. Geophysical Journal International 281–298. http://dx.doi.org/10.1111/j.1365-246X.2008.03720.x.

Lobkis, O.I., Weaver, R.L., 2001. On the emergence of the Green's function in the correlations of a diffuse field. Journal of the Acoustical Society of America 110, 3011–3017. http://dx.doi.org/10.1121/1.1417528.

Marzorati, S., Bindi, D., 2008. Characteristics of ambient noise cross correlations in Northern Italy within the frequency range of 0.1–0.6 Hz. Bulletin of the Seismological Society of America 98 (3), 1389–1398. http://dx.doi.org/10.1785/0120070140.

Mechie, J., Abu-Ayyash, K., Ben-Avraham, Z., El-Kelani, R., Qabbani, I., Weber, M., DESIRE Group, 2009. Crustal structure of the southern Dead Sea basin derived from project DESIRE wide-angle seismic data. Geophysical Journal International 178, 457–478, doi: 10.1111/j.1365-246X.2009.04161.

Mohsen, A., Asch, G., Mechie, J., Kind, R., Hofstetter, R., Weber, M., Stiller, M., Abu-Ayyash, K., 2011. Crustal structure of the Dead Sea Basin (DSB) from a receiver function analysis. Geophysical Journal International 184, 463–476. http://dx.doi.org/10.1111/j.1365-246X.2010.04853.x.

Pedersen, H.A., Krüger, F., SVEKALAPKO Seismic Tomography Working Group, 2007. Influence of the seismic noise characteristics on noise correlations in the Baltic shield. Geophysical Journal International 168, 197–210.

Quennell, A.M., 1958. The structural and geomorphic evolution of the Dead Sea rift. Geological Society of London-Quarterly Journal 114, 2–24.

Reches, Z., 1987. Mechanical aspects of pull-apart basins and push-up swells with applications to the Dead Sea Transform. Tectonophysics 141, 75–88.

Rickett, J., Claerbout, J., 1999. Acoustic daylight imaging via spectral factorization: helioseismology and reservoir monitoring. Leading Edge 18, 957–960.

Ritzwoller, M.H., Levshin, A.L., 1998. Eurasian surface wave tomography: group velocities. Journal of Geophysical Research 103 (B3), 4839–4878.

Sabra, K.G., Gerstoft, P., Roux, P., Kuperman, A.W., Fehler, C.M., 2005a. Extracting time-domain Green's function estimates from ambient seismic noise. Geophysical Research Letters 32, pp. L03 310-1–L03 310-5.

Sabra, K.G., Gerstoft, P., Roux, P., Kuperman, A.W., Fehler, C.M., 2005b. Surface wave tomography from microseisms in southern California. Geophysical Research Letters 32, pp. L14 311-1–L14 311-4.

Sánchez-Sesma, F.J., Campillo, M., 2006. Retrieval of the Green's function from cross correlation: the canonical elastic problem. Bulletin of the Seismological Society of America 96, 1182–1191.

Sánchez-Sesma, F.J., Pérez-Ruiz, J.A., Luzón, F., Campillo, M., Rodríguez-Castellanos, A., 2008. Diffuse fields in dynamic elasticity. Wave Motion 45, 641–654.

Sánchez-Sesma, F.J., Weaver, R.L., Kawase, H., Matsushima, S., Luzón, F., Campillo, M., 2011. Energy partitions among elastic waves for dynamic surface loads in a semi-infinite solid. Bulletin of the Seismological Society of America 101 (4), 1704–1709.

Sagy, A., Reches, Z., Agnon, A., 2003. Hierarchic three-dimensional structure and slip partitioning in the western Dead Sea pull-apart. Tectonics 22 (1), 1004. http://dx.doi.org/10.1029/2001TC001323.

Saygin, E., Kennett, B.L.N., 2010. Ambient seismic noise tomography of Australian continent. Tectonophysics 481, 116–125. http://dx.doi.org/10.1016/j.tecto.2008.11.013.

Schimmel, M., Stutzmann, E., Gallart, J., 2011. Using instantaneous phase coherence for signal extraction from ambient noise data at a local to a global scale. Geophysical Journal International 184, 494–506. http://dx.doi.org/10.1111/j.1365-246X.2010.04861.x.

Schuster, G., 2009. Seismic Interferometry. Cambridge University Press, Cambridge.

Shapiro, N.M., Campillo, M., 2004. Emergence of broadband Rayleigh waves from correlations of the ambient seismic noise. Geophysical Research Letters 31, L07614. http://dx.doi.org/10.1029/2004GL019491.

Silveira, G., Afonso Dias, N.A., Villaseñor, A., 2013. Seismic imaging of the western Iberian crust using ambient noise: Boundaries and internal structure of the Iberian Massif. Tectonophysics. http://dx.doi.org/10.1016/j.tecto.2012.12.025.

Snieder, R., 2004. Extracting the Green's function from the correlation of coda waves: a derivation based on stationary phase. Physical Review E 69, 046610-1–046 610-8.

Snieder, R., Miyazawa, M., Slob, E., Vasconcelos, I., 2009. A comparison of strategies for seismic interferometry. Surveys In Geophysics 30, 503–523.

Stankiewicz, J., Ryberg, T., Haberland, C., Fauzi, Natawidjaja, D., 2010. Lake Toba volcano magma chamber imaged by ambient seismic noise tomography. Geophysical Research Letters 37, L17306. http://dx.doi.org/10.1029/2010GL044211.

Stankiewicz, J., Weber, M.H., Mohsen, A., Hofstetter, R., 2012. Dead Sea Basin imaged by ambient seismic noise tomography. Pure and Applied Geophysics 169, 615–623.

Stehly, L., Fry, B., Campillo, M., Shapiro, N.M., Guilbert, J., Boschi, L., Giardini, D., 2009. Tomography of the Alpine region from observations of seismic ambient noise. Geophysical Journal International 178, 338–350, doi: 10.1111/j.1365-246X.2009.04132.

Ten Brink, U.S., Ben-Avraham, Z., Bell, R.E., Hassouneh, M., Coleman, D.F., Andreasen, G., Tibor, G., Coakley, B., 1993. Structure of the Dead Sea pull-apart basin from gravity analyses. Journal of Geophysical Research, vol. B12, 21877–21894.

Ten Brink, U.S., Al-Zoubi, A.S., Flores, C.H., Rotstein, Y., Qabbani, I., Harder, S.H., Keller, G.R., 2006. Seismic imaging of deep low-velocity zone beneath the Dead

Sea basin and transform fault: implications for strain localization and crustal rigidity. Geophysical Research Letters 33, L24314. http://dx.doi.org/10.1029/2006GL027890.

Villaseñor, A., Yang, Y., Ritzwoller, M.H., Gallart, J., 2007. Ambient noise surface wave tomography of the Iberian península: Implications for shallow seismic structure. Geophysical Research Letters 34, L11304. http://dx.doi.org/10.1029/2007GL030164.

Wapenaar, K., 2004. Retrieving the elastodynamic Green's function of an arbitrary inhomogeneous medium by cross correlation. Physical Review Letters 93 (254), 301. http://dx.doi.org/10.1103/PhysRevLett.93.254301.

Wapenaar, K., Draganov, D., Robertsson, J.O.A., 2008. Seismic interferometry: history and present status. In: SEG Geophysics Reprints Series, 26, Society of Exploration Geophysics, Tulsa, OK.

Weaver, R.L., Lobkis, I.O., 2004. Diffuse fields in open systems and the emergence of the Green's function. Journal of the Acoustical Society of America 116, 2731–2734.

Weber and, M.H., DESERT Group, 2004. The crustal structure of the Dead Sea transform. Geophysical Journal International 156, 655–681. http://dx.doi.org/10.1111/j.1365-246X.2004.02143.x.

Weber, M., Abu-Ayyash, K., Abueladas, A., Agnon, A., Alasonati- Tašárová, Z., Al-Zubi, H., Babeyko, A., Bartov, Y., Bauer, K., Becken, M., Bedrosian, P.A., Ben-Avraham, Z., et al., 2009. Anatomy of the Dead Sea transform from lithospheric to microscopic scale. Reviews of Geophysics 47 (2). http://dx.doi.org/10.1029/2008RG000264.

Yang, Y., Ritzwoller, M.H., 2008. Characteristics of ambient seismic noise as a source for surface wave tomography. Geochemistry, Geophysics, Geosystems 9 (2), Q02008. http://dx.doi.org/10.1029/2007GC001814.

Yang, Y., Li, A., Ritzwoller, M.H., 2008. Crustal und uppermost mantle structure in southern Africa revealed from ambient noise and teleseismic tomography. Geophysical Journal International 174, 235–248. http://dx.doi.org/10.1111/j.1365-246X.2008.03779.x.

Yao, H., van der Hilst, R.D., 2009. Analysis of ambient noise energy distribution and phase velocity bias in ambient noise tomography, with application to SE Tibet. Geophysical Journal International 179, 1113–1132. http://dx.doi.org/10.1111/j.1365-246X.2009.04329.x.

Zak, I., Freund, R., 1981. Asymmetry and basin migration in the Dead Sea Rift. Tectonophysics 80, 27–38.

Zheng, S., Sun, X., Song, X., Yang, Y., Ritzwoller, M.H., 2008. Surface wave tomography of China from ambient seismic noise correlation. Geochemistry, Geophysics, Geosystems 9 (5). http://dx.doi.org/10.1029/2008GC001981.